Optical spectroscopy of Pr^{3+} in $KGd(WO_4)_2$ single crystals

2000 J. Phys.: Condens. Matter 12 8531

(http://iopscience.iop.org/0953-8984/12/39/315)

J. Phys.: Condens. Matter **12** (2000) 8531–8550. Printed in the UK PII: S0953-8984(00)13027-9

Optical spectroscopy of Pr^{3+} in $KGd(WO_4)_2$ single crystals

C Zaldo†‖, M Rico†, C Cascales†, M C Pujol‡, J Massons‡, M Aguiló‡, F Díaz‡ and P Porcher§

† Instituto de Ciencia de Materiales de Madrid, Consejo Superior de Investigaciones Científicas, Cantoblanco, 28049 Madrid, Spain

‡ Laboratori de Fisica Aplicada i Cristal.lografia, Universitat Rovira i Virgili, 43005 Tarragona, Spain

§ Laboratoire de Chimie Appliquée de l'Etat Solide, UMR 7574-CNRS, ENSCP, 11 rue Pierre et Marie Curie, F-75231 CX05, France

E-mail: cezaldo@icmm.csic.es

Received 3 April 2000, in final form 19 May 2000

Abstract. The polarized optical absorption (OA) and photoluminescence of Pr^{3+} doped $KGd(WO_4)_2$ (KGW) single crystals have been measured at selected temperatures between 7 and 300 K. For the studied Pr concentrations, [Pr] $= 0.03 \times 10^{20}$–1.9×10^{20} cm^{-3}, a unique site is observed. 74 energy levels were experimentally determined for this site and labelled with the appropriate A or B irreducible representations corresponding to the C_2 symmetry of the Gd point site in KGW. The set was fitted to a Hamiltonian of adjustable parameters including free-ion as well as real B_q^k and complex S_q^k crystal-field parameters. A good simulation of the experimental crystal field energies was achieved with a root mean square deviation $\sigma = 15.3$ cm^{-1}. Distortions in the oxygen bonds to Pr^{3+} are found to contribute to the broadening of some OA bands, particularly those related to the $^1D_2$ multiplet. The OA edge is determined by the interconfigurational 4f$\rightarrow$ 4f^{1}5d^1 Pr^{3+} transition peaking at 34 200 cm^{-1}. From the average 300 K OA cross sections the radiative lifetimes of the Pr^{3+} multiplets have been calculated considering the standard and modified Judd–Ofelt (JO) theories. A better agreement with the experimental results is obtained by the standard theory: the average JO parameters obtained at $\bar{\Omega}_2 = 12.0 \times 10^{-20}$ cm^2, $\bar{\Omega}_4 = 8.15 \times 10^{-20}$ cm^2 and $\bar{\Omega}_6 = 2.64 \times 10^{-20}$ cm^2. Electrons excited to the $^3P_0$ multiplet decay very efficiently to the $^1D_2$ multiplet even at 15 K. In samples with [Pr] $\geqslant 0.3 \times 10^{20}$ cm^{-3} the excitation of the $^1D_2$ multiplet decays non-radiatively by an electric dipole–dipole transfer between Pr neighbours.

1. Introduction

Monoclinic double tungstate single crystals, with chemical formula $KRE(WO_4)_2$, RE being the rare earths, are currently receiving attention as hosts for self-induced frequency shifting [1]. $KRE(WO_4)_2$ (hereafter KRW) matrices have large values of the χ^3 non-linear constant describing the Raman coupling. Further, the $^4F_{3/2} \rightarrow {}^4I_{11/2}$ emission of Nd^{3+} in $KGd(WO_4)_2$ (hereafter KGW) is as efficient as in the widely used YAG host, but it has a lower laser threshold in KGW [2]. Laser emission in the 1.06–1.07 μm region has also been observed at room temperature using the $^1D_2 \rightarrow {}^3F_4$ Pr^{3+} emission in KRW crystals [3]. Moreover, the $^1G_4 \rightarrow {}^3H_5$ transition of Pr^{3+} is of particular interest in relation to the 1.3 μm window of the optical telecommunication because of the large cross section and lifetime expected [4].

The optical spectroscopy of Pr in KGW has been reported only at temperatures equal to or above 77 K [5, 6]. For the unambiguous determination of the energy levels the study at 10 K

‖ Corresponding author.

0953-8984/00/398531+20$30.00

or below is required in order to avoid thermal population of excited sublevels of the ground $^3H_4$ multiplet.

The crystal field model [7, 8] has been successfully used in the analysis of $4f^N$ configurations of lanthanides in solids. A satisfactory simulation can only be achieved if the number and quality of the operators are adequate. From this point of view, the interest of Pr^{3+} is due to the relatively sparse number of possible energy levels and the infrequent overlap of different $^{2S+1}L_J$ multiplets which, together with their low total angular moment (J) degeneracy, facilitates the interpretation of the optical absorption (OA) and emission spectra.

In this work we have experimentally determined at 7 K the energy position of 74 praseodymium levels and their experimental polarization character. This set of Stark levels has been labelled A or B according to the C_2 point site symmetry. The energy level scheme has been fitted by least squares minimization to a Hamiltonian including free ion and crystal-field interactions. The broadening of the $^1D_2$ multiplet is discussed in terms of different crystal-field interactions caused by oxygen distortions in the Pr^{3+} neighbourhood. The room temperature OA cross sections have been measured and used to calculate the radiative lifetimes according to the Judd–Ofelt (JO) theory [9, 10]. These results are compared with experimental lifetimes. The role of Pr concentration in the optical properties is also discussed.

2. KGW structure and principal axes

The KGW crystal is monoclinic, space group $C2/c$ (No 15) [11]. The lattice parameters of the unit cell are $a = 10.652(4)$ Å, $b = 10.374(6)$ Å, $c = 7.582(2)$ Å, $\beta = 130.80(2)^\circ$ and $Z = 4$. The b-axis is parallel to the binary C_2 symmetry element.

Trivalent rare earths are assumed to substitute Gd^{3+}. Gadolinium is coordinated with eight oxygens forming a distorted square antiprism, with four different Gd–O distances, namely Gd–O1 = 2.325 Å, Gd–O2 = 2.271 Å and Gd–O3 = 2.650 and 2.371 Å. The local symmetry of Gd and its first coordination sphere only contain a C_2 axis parallel to the b axis of the lattice.

The principal axis of the optical indicatrix with lowest refractive index is labelled p and is parallel to the crystallographic b axis [11]. The principal axis with the highest refractive index is labelled g and is in the ac place forming 21.5° with the c axis in the clockwise direction when looking from the positive end of the b axis. Finally, the principal axis with intermediate refractive index is labelled m and is in the ac plane orthogonal to g.

3. Experimental techniques

KGW single crystals have been grown by the top seeded solution growth (TSSG) method using a $K_2W_2O_7$ solvent. Crystal growth experiments were carried out at 920–950 K at the 31.41 K_2O : 1.92 Gd_2O_3 : 66.67 WO_3 point of the phase diagram (11.5/88.5 solute/solvent molar ratio). In order to obtain samples with different praseodymium concentration, four different $Pr_2O_3/(Gd_2O_3+Pr_2O_3)$ ratios of gadolinium oxide substitution were fixed 0.001, 0.01, 0.03 and 0.05 (hereafter named 0.1%, 1%, 3% and 5% respectively). Details of the growth procedure have been given previously [11, 12]. The Pr concentrations of the three latter samples have been determined by electron probe microanalysis, using CAMECA Camebax SX50 equipment, being [1% Pr]= 0.3×10^{20} cm^{-3}, [3% Pr]= 0.9×10^{20} cm^{-3} and [5% Pr]= 1.9×10^{20} cm^{-3}. The segregation coefficient of praseodymium was 0.52. Samples were oriented by x-ray diffraction and polished for optical measurements.

OA and photoluminescence were performed in the 7–300 K temperature range using flowing liquid helium and He closed-cycle cryostats connected to suitable temperature controllers.

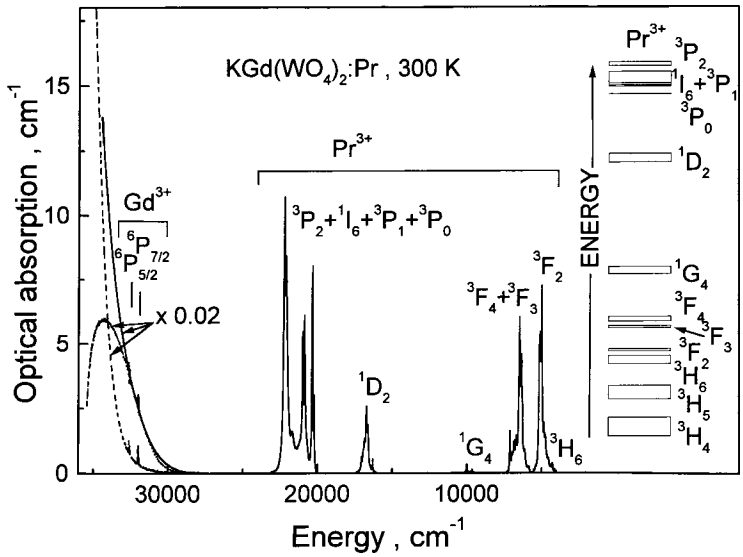

Figure 1. Room temperature optical absorption of 5% Pr doped $KGd(WO_4)_2$ single crystals. The spectrum corresponding to an undoped sample is given for comparison (dashed line). The spectra in the 25 000–35 000 cm^{-1} region have been recorded using 66 μm thin samples. The dotted line shows the difference in the absorption edge region between undoped and Pr doped KGW recorded at 7 K. The spectra in the absorption edge region are multiplied by 0.02 to ease the display. The energy positions of the Pr^{3+} multiplets are schematically given for reference.

Absorption was recorded in a Varian 5E spectrophotometer. Continuous wave (cw) photoluminescence was excited with the ultraviolet multiline emission of a coherent 5 W Ar laser, model Innova 300. The excitation light intensity was in the 10–200 mW range: this excitation includes lines at 27 548, 28 490, 29 779, 29 895 and 29 976 cm^{-1}. The emission was analysed with a Spex 340E spectrometer ($f = 34$ cm) and detected with a cooled R928 Hamamatsu photomultiplier ($\lambda = 185$–900 nm) or with a Ge photodiode, model ADC-403 IR, cooled to 77 K ($\lambda = 1.0$–1.7 μm). The detector signals were recorded by using a lock-in amplifier.

Lifetimes measurements were excited with a Spectra Physics optical parametric system model MOPO-730. The system provides pulses with a fall time of 5 ns. $^3P_0 \rightarrow {}^3H_5$ and $^1D_2 \rightarrow {}^3H_4$ emissions were monitored by using a Spex 500M ($f = 50$ cm) spectrometer and detected with a GaInAs photomultiplier connected to a Tektronix 2440 digital oscilloscope. The fall time of the detector is 2 ns.

4. Experimental results

4.1. Room temperature optical absorption and photoluminescence

The OA spectra of Pr^{3+} in KGW crystals have been measured at room temperature with light polarized parallel to the three principal axes. Figure 1 gives an average of the three spectra. At room temperature the $^1G_4$ multiplet appears poorly resolved from the background noise and some multiplets are strongly overlapped due to the thermal population of the sublevels of the ground $^3H_4$ multiplet.

In addition to the sharp lines peaking below 25 000 cm^{-1} which belong to Pr^{3+} transitions, the room temperature OA spectrum also shows narrow bands at about 32 000 and 32 600 cm^{-1}

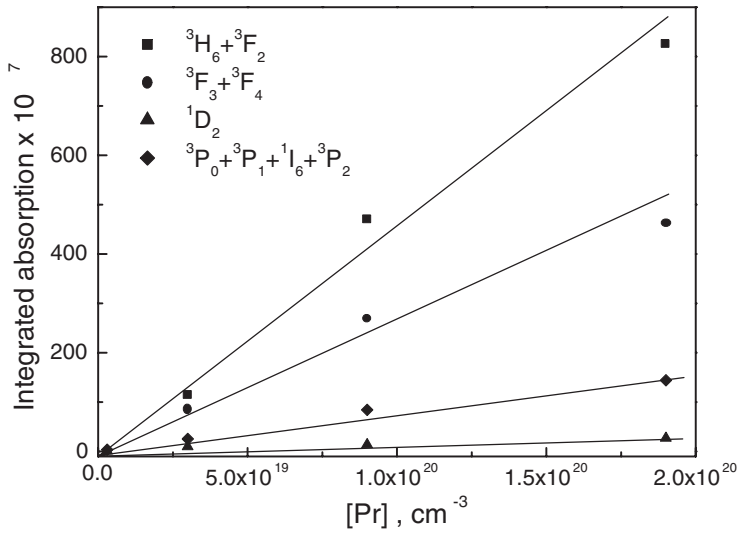

Figure 2. Averaged room temperature integrated absorption, $\int \bar{\alpha} \partial \lambda$, as a function of the total praseodymium concentration, [Pr].

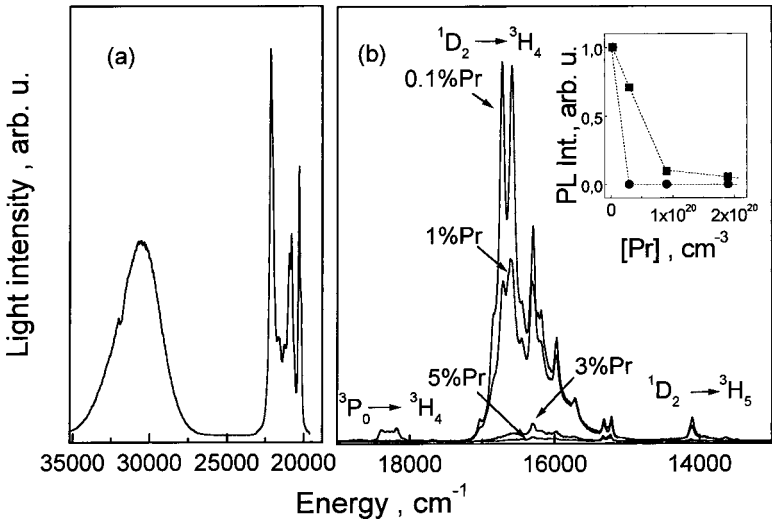

Figure 3. Room temperature photoluminescence of Pr doped $KGd(WO_4)_2$. (a) Excitation spectrum recorded with 0.1% Pr sample. $1/\lambda_{EMI} = 16\,313\ \text{cm}^{-1}$. (b) Emission spectra. $1/\lambda_{EXC} = 31\,250\ \text{cm}^{-1}$. The inset shows the integrated emission intensity of the $^3P_0$ (●) and $^1D_2$ (■) multiplets as a function of the total praseodymium concentration, [Pr].

corresponding to $^8S_{7/2} \rightarrow {}^6P_{7/2}$ and $^8S_{7/2} \rightarrow {}^6P_{5/2}$ intraconfigurational transitions of Gd^{3+} respectively [13]. Further, a broad band peaking at about $34\,200\ \text{cm}^{-1}$ induces a shifting to lower energy of the apparent absorption edge of Pr doped KGW with regards to undoped samples. This latter band is little sensitive to temperature; it has been observed in other praseodymium doped materials and sometimes attributed to Pr^{4+} [14]. We shall show later that the JO analysis yields a Pr^{3+} concentration close to the total Pr concentration, therefore the Pr^{4+}/Pr^{3+} ratio in KGW must be small and the possible presence of Pr^{4+} will be neglected.

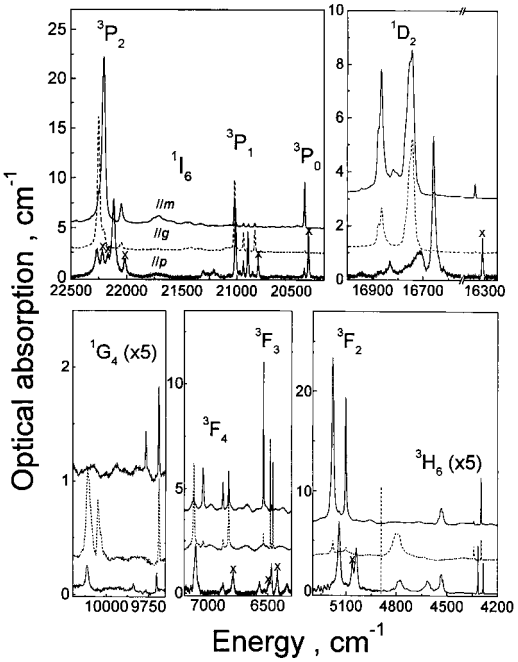

Figure 4. 7 K optical absorption of 1% Pr doped $KGd(WO_4)_2$ single crystals recorded with light polarized parallel to the three principal axes, $\parallel p$, $\parallel g$ and $\parallel m$. The spectra $\parallel g$ and $\parallel m$ have been arbitrarily shifted in the absorption axis to give clarity to the plot. Bands marked $\times$ in the $\parallel p$ spectra have a thermal origin.

The origin of this broad band is most likely due to a $4f^2 \rightarrow 4f^15d^1$ interconfigurational transition of Pr^{3+}. The energy of this transition depends on the host matrix, the absorption edge of the band moving to low energy when the crystal field increases [15]. The position of this band also determines the photoluminescence efficiency of ^3P_J multiplets and the transfer rate between $^3P_0$ and $^1D_2$ multiplets.

Figure 2 shows the dependence of the average integrated absorption $\bar{\Gamma}_{JJ'} = \int \bar{\alpha}(\lambda)\,d\lambda$ of some multiplets with the total Pr concentration. Within the experimental uncertainty, the integrated absorption scales linearly the praseodymium concentration. This allows us to calculate the Pr^{3+} concentration in the 0.1% Pr doped sample as [0.1% Pr]$= 0.03 \times 10^{20}$ cm^{-3}.

Figure 3 shows the room temperature photoluminescence of Pr doped KGW crystals. Exciting at 31 250 cm^{-1} the emission spectra of the 0.1% doped sample shows a weak band at 18 280 cm^{-1}, a much more intense emission between 15 000 and 17 000 cm^{-1} and a weak band at 14 108 cm^{-1} (see figure 3(b)). According to the previous knowledge of Pr^{3+} spectroscopy [15–17], the first emission corresponds to the $^3P_0 \rightarrow {}^3H_4$ de-excitation, the second one to the $^1D_2 \rightarrow {}^3H_4$ transition and the last one to the $^1D_2 \rightarrow {}^3H_5$ de-excitation. The $^3P_0 \rightarrow {}^3H_5$ emission is not observed at room temperature. All these emission bands are also excited by pumping the ^3P_J multiplets of Pr^{3+}. Due to the low energy distance between the ^3P_J multiplets, the excitation is thermally relaxed to the one at lowest energy, namely $^3P_0$, from which transitions to lower energy multiplets may take place. The overall emission intensity decreases with increasing Pr concentration (see the inset of figure 3(b)), but the intensity of the $^3P_0 \rightarrow {}^3H_4$ emission decreases faster than that of the $^1D_2 \rightarrow {}^3H_4$. This fact and the weakness of the $^3P_0 \rightarrow {}^3H_4$ emission indicate that the excitation of $^3P_0$ is strongly relaxed to the $^1D_2$ multiplet. In fact, this behaviour is usual in crystals where the $4f^2 \rightarrow 4f^15d^1$ Pr^{3+}

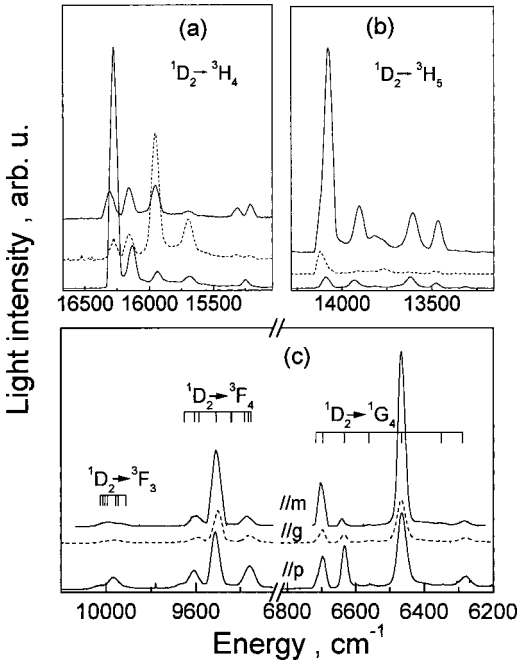

Figure 5. 7 K photoluminescence of $^1D_2$ multiplet of 1% Pr doped $KGd(WO_4)_2$ single crystals excited with unpolarized multiline ultraviolet emission of an Ar laser. The emissions have been recorded parallel to the three principal axes, $\parallel p$, $\parallel g$ and $\parallel m$ of the matrix. The spectra $\parallel g$ and $\parallel m$ have been arbitrarily shifted in the vertical axis to give clarity to the plot. The energy differences of the Stark components of the bottom multiplet deduced from absorption are given in (c) for comparison.

interconfigurational transition lies at low energy [15]. In KGW, being one of the materials with lowest transition energy, the maximum of this transition determined from the excitation spectrum lies at about 30 530 cm^{-1}.

4.2. Low temperature optical absorption and photoluminescence

Figure 4 shows the 7 K optical absorption of the 1% Pr doped KGW sample which is representative of all concentrations studied. The low temperature OA is strongly sensitive to the polarization of the light with regard to the principal axes of the matrix. Moreover, contributions arising from the thermally populated first and second excited levels of the $^3H_4$ multiplet are easily observed above 10 K. These facts, along with the strong overlap of the $^3P_1$ and $^1I_6$ multiplets and the low intensity of $^1G_4$ hamper the unambiguous determination of the energy position of the Pr^{3+} Stark levels, E_i. Nevertheless, the comparison between the four Pr concentrations available in the possible three polarization configurations and the thermal behaviour of the bands observed has allowed us to made the assignations reported in table 1.

Figure 5 shows an overview of the 7 K photoluminescence emissions arising from the de-excitation of the $^1D_2$ multiplet. The emission bands observed correspond well to those reported from Pr^{3+} in other crystalline lattices [15–17] and with the energy positions determined from OA. Some energies of the Stark sublevels of the ground ($^3H_4$) and first excited ($^3H_5$) multiplets of Pr^{3+} have been deduced from the emissions corresponding to the de-excitation of the $^1D_2$ multiplet. The results are also included in table 1.

Table 1. Pr^{3+} energy levels (cm^{-1}) in $KGd(WO_4)_2$. Observed at 7 K (E_0) and calculated (E_c) using the cfps of table 2. $\Delta = E_0 - E_c$. ‖ indicates the experimental polarization of the emission or absorption bands and IR the corresponding irreducible representations.

$^{2S+1}L_J$	IR	‖	E_0	E_c	Δ		IR	‖	E_0	E_c	Δ
$^3H_4$	B	*m*	0.1	11	−11	$^3F_4$	A	*mg*	6831	6831	0
	A	*p*	39	34	5		B		—	6850	—
	B	*mg*	144	159	−15		B	*p*	6872	6858	14
	A	*p*	172	168	4		A	*mg*	6877	6860	17
	B	*mg*	358	357	1		B	*p*	6973	6964	9
	A	*p*	370	372	−2		A	*m*	7041	7055	−14
	A		—	397	—		B	*p*	7102	7095	7
	B	*mg*	608	589	19		A	*g*	7118	7131	−13
	A	*p*	615	628	−13		A	*m*	7131	7153	−22
$^3H_5$	A		—	2184	—	$^1G_4$	B		—	9612	—
	B	*g*	2187	2196	9		A	*mg*	9688	9660	28
	A	*p*	2217	2224	−7		B	*p*	9703	9716	−13
	B	*m*	2239	2234	5		A	*m*	9766	9741	25
	A	*p*	2378	2372	6		B	*p*	9933	9933	0
	B	*mg*	2409	2411	−2		A	*g*	10 049	10 056	−7
	B		—	2463	—		A	*g*	10 110	10 126	−16
	A	*p*	2493	2482	11		B	*p*	10 114	10 126	−12
	B	*g*	2543	2548	−5		A		—	10 291	—
	A	*p*	2689	2677	12						
	B	*m*	2706	2689	17	$^1D_2$	A	*m*	16 347	16 346	1
							B	*p*	16 654	16 659	−6
$^3H_6$	B	*p*	4284	4307	−23		A	*mg*	16 750	16 745	5
	A	*mg*	4297	4310	−13		A	*mg*	16 866	16 866	0
	B	*p*	4316	4334	−18		B		—	17 014	—
	A	*mg*	4341	4341	0						
	A	*m*	4531	4527	4	$^3P_0$	A	*m*	20 380	20 385	−5
	B	*p*	4534	4541	−7						
	B	*p*	4603	4597	6						
	A		—	4612	—	$^1I_6$	A			20 828	—
	A		—	4684	—	$^1I_6$	A	*g*	20 836	20 832	4
	B	*p*	4775	4752	23	$^3P_1$	B	*p*	20 899	20 878	21
	A	*g*	4796	4784	12	$^1I_6$	A	*g*	20 940	20 937	3
	A	*m*	4959	4957	2	$^1I_6$	B	*p*	20 942	20 936	6
	B	*p*	4965	4965	0	$^3P_1$	B	*p*	21 013	21 013	0
						$^3P_1$	A	*mg*	21 022	21 025	−4
$^3F_2$	B	*p*	5038	5048	−10	$^1I_6$	B	*p*	21 209	21 236	−27
	A	*mg*	5100	5094	6	$^1I_6$	B		—	21 248	—
	B	*p*	5141	5127	13	$^1I_6$	A		—	21 383	—
	A	*mg*	5179	5179	0	$^1I_6$	B		—	21 465	—
	A	*mg*	5192	5212	−20	$^1I_6$	A	*mg*	21 473	21 477	−4
						$^1I_6$	B		—	21 695	—
$^3F_3$	A	*mg*	6456	6432	24	$^1I_6$	A	*m*	21 708	21 690	18
	B	*p*	6468	6469	−1	$^1I_6$	A		—	21 795	—
	A	*mg*	6477	6476	1	$^1I_6$	B		—	21 795	—
	B	*p*	6489	6483	6						
	B	*p*	6525	6533	−8	$^3P_2$	A	*mg*	22 049	22 038	11
	A	*mg*	6535	6539	−4		B	*p*	22 117	22 090	27
	B	*p*	6569	6583	−14		A	*mg*	22 204	22 233	−29
							A	*g*	22 252	22 274	−22
							B	*p*	22 267	22 266	1
						$^1S_0$	A		—	45 950	—

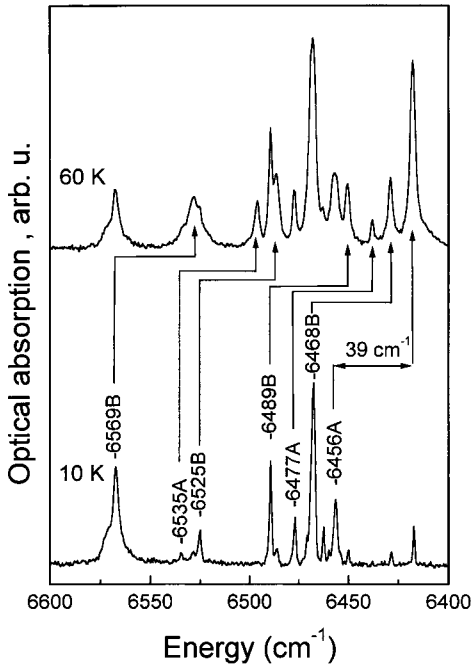

Figure 6. Thermal evolution of the unpolarized OA associated with the $^3H_4 \rightarrow {}^3F_3$ transition of Pr^{3+} in 1% Pr doped $KGd(WO_4)_2$. The spectrum at 10 K mainly shows the transitions from the ground $^3H_4$ Stark level labelled by their energy and IR. The additional bands observed at 60 K arise from the thermal population of the first excited $^3H_4$ Stark level. The arrows indicate band pairs starting from the ground and first excited levels and shifted by 39 cm^{-1}.

The energy of the first excited Stark level has been determined from the thermal evolution of the unpolarized OA or Pr^{3+} (see figure 6). It is worth noting that the ground and first excited Stark levels correspond to different IR (see table 1); therefore, transitions from these two levels to a single upper one cannot be simultaneously observed in the same polarized OA spectrum. Figure 6 shows the growth with temperature of a band set displaced 39 cm^{-1} to low energy with regards to the band set at 10 K. This energy shift corresponds to the gap between the ground and first excited Stark levels. In figure 6 we have shown $^3H_4 \rightarrow {}^3F_3$ transitions because their small bandwidths (≈2–5 cm^{-1} at 7 K) allow a clear distinction between both band sets, although similar results have been found for all other transitions studied (namely, $^3H_4 \rightarrow {}^3F_2$, $^3F_3$, $^3F_4$, $^1D_2$, $^3P_0$, $^1I_6 + {}^3P_1$). The assignations of table 1 can be compared to those made previously at 77 K [5, 6]. A rough agreement can be found between all works, but the number of levels reported in the present work is larger and the energies are determined with more confidence due to the lower temperature used for the measurement.

Significant differences have been found in the 7 K optical absorption bandwidth of different multiplets (see figure 4). The largest bandwidth is observed in sublevels of the $^1D_2$ multiplet, being about 30–40 cm^{-1}, while the smallest one corresponding to the $^3F_3$ sublevels is 2 cm^{-1}. Moreover, the $^1D_2$ sublevels show a structure which may not be observed in the $^3F_3$ ones (compare figures 6 and 7). As shown in figure 7, the structure observed in the $^1D_2$ multiplet is not related to a thermal effect: most likely it corresponds to the contribution of several Pr^{3+} centres in slightly different crystal fields. The evolution of the $^1D_2$ sublevels also shows the thermal population of the second excited Stark level at 144 cm^{-1}, which is responsible for the growth of a band at 16 618 cm^{-1}.

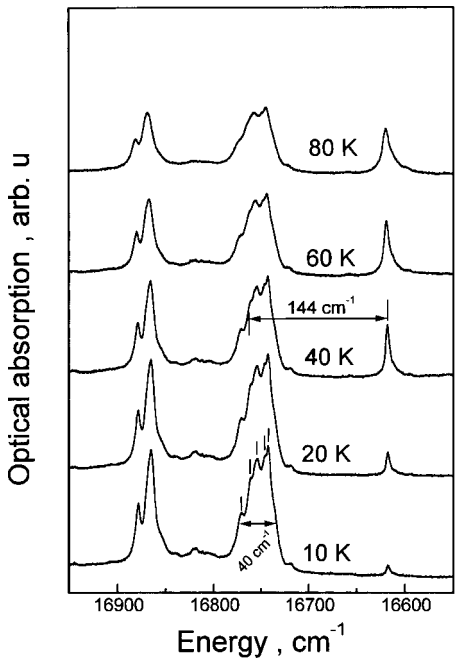

Figure 7. Temperature dependence of the $\|$ *m* polarized optical absorption associated to the $^3H_4 \rightarrow {}^1D_2$ transition of Pr^{3+} in 1% Pr doped $KGd(WO_4)_2$. The temperature of measurement is indicated on the spectra.

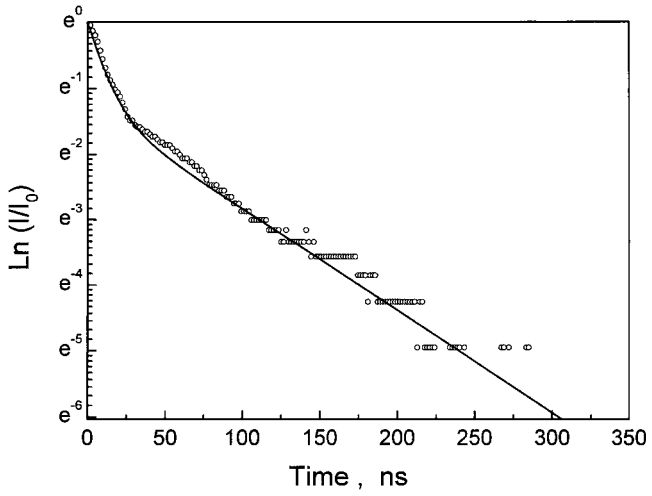

Figure 8. 15 K light intensity decay of the $^3P_0$ multiplet obtained in 0.1% Pr doped $KGd(WO_4)_2$. $1/\lambda_{EXC} = 20\,380\ cm^{-1}$, $1/\lambda_{EMI} = 17\,730\ cm^{-1}$. The symbols are the experimental results and the line is the fit assuming the addition of two exponential decays with time constants of 10 ns and 66 ns respectively.

4.3. Lifetime measurements

Figure 8 shows the experimental decay of the $^3P_0$ multiplet measured by pumping at $20\,380\ cm^{-1}$ and monitoring the $^3P_0 \rightarrow {}^3H_5$ emission at $17\,730\ cm^{-1}$. The experiments

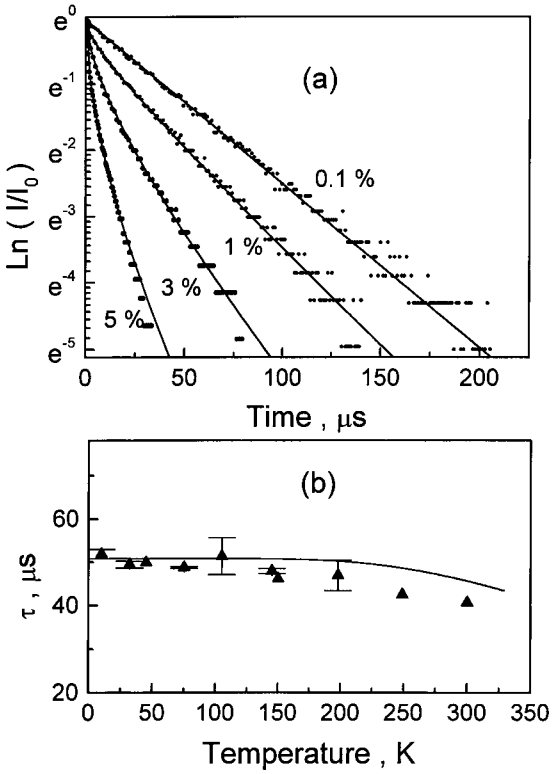

Figure 9. (a) Light intensity decays of the $^1D_2$ photoluminescence of Pr^{3+} in $KGd(WO_4)_2$ for different praseodymium concentrations. $1/\lambda_{EXC} = 16\,863$ cm^{-1}. $1/\lambda_{EMI} = 15949$ cm^{-1}. The points are experimental results. The solid line of the 0.1% doped sample shows the exponential fit. The solid curves of other samples are the fits obtained using the Inokuti–Hirama model with $s = 6$. (b) Temperature dependence of the experimental lifetime (▲) of the $^1D_2$ multiplet measured in 0.1% Pr doped $KGd(WO_4)_2$. $1/\lambda_{EXC} = 16\,863$ cm^{-1}. $1/\lambda_{EMI} = 15\,948$ cm^{-1}. The line is the dependence predicted by equation (8) using eight phonons of 901 cm^{-1}.

were performed on the 0.1% Pr doped sample in order to minimize concentration effects. At 15 K the light decay can be fit by two exponential decays with lifetimes of 10 and 65 ns. The short lived one can be influenced by the system detection response and it will be ignored. At 30 K the decay becomes faster and the long-lived one does not appear. Above this temperature the emission intensity decreases below of our detector sensitivity.

The 300 K photoluminescence lifetime of the $^1D_2$ multiplet has been excited at 16 863 cm^{-1} and measured at 15 949 cm^{-1}. Figure 9(a) shows the room temperature results of the four Pr concentrations available. An exponential decay is only obtained for the lowest Pr concentration. In that case the 300 K radiative lifetime obtained is 40.7 μs. Figure 9(b) shows the lifetime temperature dependence of the $^1D_2$ multiplet for the 0.1% Pr doped sample measured in the 10–300 K temperature range. All the decays obtained are exponential and the lifetime of the $^1D_2$ multiplet increases up to about 51 μs at the lowest reached temperature, namely 10 K.

The 300 K $^1D_2$ lifetime determined in this work (40.7 μs) is larger than that reported previously, namely 33.7 μs [5]. This difference is due to the larger Pr concentration ([Pr] = 1%) used previously. In fact, if the non-exponential character of our 1% Pr doped sample were ignored the rough lifetime calculation would yield a value similar to that reported previously.

5. Discussion

5.1. Crystal-field model

The central-field approximation allows us to consider the Hamiltonian of the $4f^2$ configuration of Pr^{3+} as a sum of the free ion, H_{FI}, and the crystal field, H_{CF}, Hamiltonians. H_{FI} can be written as [18]

$$H_{FI} = H_0 + \sum_{k=0,1,2,3} E^k e_k + \zeta_{4f} A_{SO} + \alpha L(L+1) + \beta G(G_2) + \gamma G(R_7) + \sum_{k=0,2,4} M^k m_k + \sum_{i=2,4,6} P^i p_i. \quad (1)$$

H_0 stands for the spherically symmetric one-electron term. E^k are the Racah parameters. ζ_{4f} is the spin–orbit coupling constant. α, β and γ are the Trees parameters associated with the angular moment component L and with the Casimir operators G for the groups G_2 and R_7, respectively. M^k are the Marvin integrals and, finally, the electrostatically correlated spin–orbit interactions are described by the P^i integrals.

Following the Wybourne formalism [7], H_{CF} is expressed as a sum of products of spherical harmonics and crystal-field (B_q^k and S_q^k) parameters (cfps),

$$H_{CF} = \sum_{k=2}^{4,6} \sum_{q=0}^{k} [B_q^k (C_q^k + (-1)^q C_{-q}^k) + \mathrm{i} S_q^k (C_q^k - (-1)^q C_{-q}^k)]. \quad (2)$$

For the C_2 symmetry of the RE^{3+} site in KGW, the serial development of the crystal field potential involves 15 non-zero cfps, reduced to 14 by a proper choice of the reference axis system, which cancels S_2^2. This large number of adjustable parameters may produce uncertainty [19]. The free-ion parameters do not vary much for a lanthanide ion in different systems, to reduce the uncertainty the free-ion parameters can be taken from the literature [18]. In contrast, the cfps show a large variation depending on the host.

Previous crystal field calculations for $4f^2$ and $4f^3$ configurations of Pr^{3+} and Nd^{3+} in KGW and KYW matrices [6] have been started with cfps obtained from the superposition model [20]. In the present work, we have applied the *simple overlap model* (SOM) [21] to obtain the initial set of cfps from the crystallographic structure.

In the SOM model, it is assumed that the interaction energy of RE^{3+} in a chemical environment is produced by an electrostatic potential created by charges uniformly distributed over small regions centred around the mid-point of the R_ℓ distances from RE^{3+} to the ligand, ℓ, R_0 being the shortest distance. The charge in each region is proportional to the total overlap integral ρ between the 4f and the s and p orbitals of the RE^{3+} and ℓ, respectively. The cfps are written as

$$B_q^k = \langle r^k \rangle \sum_\ell \rho_\mu \left(\frac{2}{1 \pm \rho_\ell} \right)^{k+1} A_q^k(\ell) \qquad \rho_\ell = \rho_0 \left(\frac{R_0}{R_\ell} \right)^{3.5}. \quad (3)$$

The sum over ℓ is restricted to the first neighbours. A_q^k is the lattice sum and it takes into account the symmetry properties of the RE^{3+} site, including the effective charge attributed to each ligand. To obtain significant cfps γ was fixed, since the $^1S_0$ level in which its effect has real importance is not observed. M^k and P^i cannot be freely varied [19]. Table 2 summarizes the ratios used in this work.

The correct procedure for the simulation of the energy level scheme of Pr^{3+} involves the simultaneous treatment of H_{FI} and H_{CF} using the untruncated basis set of wavefunctions. The best fit of parameters was obtained by the least-squares refinement between the observed and calculated energy level values through a minimization of the root-mean-square (rms) function

Table 2. Free ion and cfps (cm^{-1}) for Pr^{3+} in $KGd(WO_4)_2$ crystals. Italic characters indicate cfps calculated from SOM. Values in parentheses refer to e.s.d. in the indicated parameter. Values in brackets were not allowed to vary in the parameter fitting. The crystal field strength parameter S_T is defined [24] as $S_T = \left[\frac{1}{3}\sum_k S_k^2\right]^{1/2}$ $\quad S_k = \left\{\frac{1}{2k+1}\left[(B_0^k)^2 + 2\sum_q (B_q^k)^2 + (S_q^k)^2\right]\right\}^{1/2}$.

E^0		9546 (1)
E^1		4469 (2)
E^2		21.54 (1)
E^3		455.5 (1)
α		22.09 (5)
β		−701 (6)
γ		[1470]
ζ		743.5 (7)
$M^{0,a}$		[1.00]
$P^{2,b}$		[250]
B_0^2	*558*	303 (9)
B_2^2	*346*	311 (8)
B_0^4	*−1019*	−1387 (21)
B_2^4	*361*	50 (26)
S_2^4	*−955*	−1029 (16)
B_4^4	*226*	118 (28)
S_4^4	*315*	487 (19)
B_0^6	*−292*	−291 (35)
B_2^6	*280*	83 (33)
S_2^6	*−145*	−248 (28)
B_4^6	*109*	−23 (35)
S_4^6	*−34*	−219 (27)
B_6^6	*−221*	−352 (26)
S_6^6	*215*	141 (42)
S_2	*332*	239
S_4	*617*	711
S_6	*197*	216
S_T	*420*	451
l Stark levels		74
σ (cm^{-1})		15.3
Residue		12 408.9

[a] M^0, M^2, M^4 were constrained by the ratios $M^2 = 0.5625M^0$, $M^4 = 0.3125M^0$.
[b] P^2, P^4, P^6 were constrained by $P^4 = 0.75P^2$, $P^6 = 0.50P^2$.

$\sigma = [\Sigma(\Delta_i)^2/(l-t)]^{1/2}$, where Δ_i is the difference between observed and calculated energies, l is the number of levels and t is the number of parameters freely varied. The simulation was performed by the programs REEL and IMAGE [22].

5.2. Results of the crystal field simulation

The $4f^2$ ground configuration of Pr^{3+} gives rise to 13 states which all, except for $^1S_0$, are situated below 25 000 cm^{-1}. The crystal-field interaction allows electric dipole ED transitions and lifts the $(2J + 1)$ degeneracy of the $^{2S+1}L_J$ free-ion levels of Pr^{3+}, which are split into Stark components characterized by irreducible one-dimensional representations, IR, **A** and **B** (Γ_1 and Γ_2 in Bethe's nomenclature). For the C_2 point site symmetry of Gd in KGW: $J = 0$, **A**; $J = 1$, **A + 2B**; $J = 2$, **3A + 2B**; $J = 3$, **3A + 4B**; $J = 4$, **5A + 4B**; $J = 5$, **5A + 6B**, and $J = 6$, **7A + 6B**. Since the principal p axis coincides with the twofold crystallographic axis of

C_2, the ED selection rules for transitions between the Stark components are as follows: A→A (p polarization), A↔B (m, g polarizations), B→B (p polarization). The $^3H_4 \leftrightarrow {}^3H_5$ Pr^{3+} transitions have a non-negligible magnetic dipole MD character [23]. The selection rules are, in this case, A→A (R_p polarization), A↔B (R_m, R_g polarizations) and B→B (R_p polarization). Therefore, from the measurements with linear polarized light the ED or MD character of the transition cannot be ascertained.

It must be noted that the intensity changes of the OA measured parallel to the m and g principal axes sometimes are much larger than those expected from the refractive index dependence of the oscillator strengths (see equation (5)). However, as a first approximation they will be hereafter considered as equivalent.

The IR of $^3P_0$ ($J = 0$) is A, and since it is seen in an m absorption spectrum, the ground level where this transition has its origin is B. Thus, transitions from the ground Stark level to A levels will be observed in m and g spectra, and those to B levels in p spectra. The 74 energy levels summarized in table 1 have been labelled A or B according to the experimental results and the discussion above. It is worth mentioning that the polarization characters of the $^3H_4$ and $^3H_5$ multiplets have been deduced from photoluminescence emission of the $^1D_2$ multiplet. As the lowest energy $^1D_2$ Stark level is A, the experimental polarization of these two multiplets is reversed with regards to those observed in OA experiments.

In the fitting process, the $4f^2$ configuration states (and thus the observed energy levels), have been distributed in two submatrices, according to the values of the crystal quantum numbers $\mu = 0$ and $\mu = 1$ [7]. For the C_2 point symmetry each submatrix is associated with only one IR, A or B, which makes the polarization assignments easier. The simulation of these crystal field levels was carried out with a very satisfactory rms deviation, $\sigma = 15.3\ cm^{-1}$. Even more important, no large discrepancies between the calculated and experimental values of individual energy levels are observed, with the exception of the $^3P_2$ multiplet and an $^1I_6$ sublevel at 21 295 cm^{-1}, which could not be fitted. It is also worth noting that a weak absorption of 9838 cm^{-1} ($^1G_4$) could not be fitted either in this work or in a previous work [6]. Table 2 summarizes the free-ion and crystal-field parameters of the best fit. The good quality of the fit is verified also by the low standard deviation values of the parameters. Table 2 also contains the starting cfps obtained from SOM, and the comparison of crystal field strengths S_k [24] for both SOM and fitted parameters. There is a general similarity between these strengths and both sets of real cfps. In contrast, complex parameters from empirical methods are usually very difficult to correctly simulate: even their signs cannot be fixed, as in the present case.

In the case of Pr^{3+} the crystal-field splitting of the $^1D_2$ state has been notoriously badly simulated in most studied lattices. It has been shown [25] that the simulation of $^1D_2$ can be improved by taking into account either (i) the configuration interaction between the ground $4f^2$ and the lowest $4f^15d^1$ (through off cfps), lying very low in energy, or $4f^16p^1$ (through even cfps) configurations, or (ii) the spin and/or orbitally correlated crystal field. Our simulation for Pr^{3+} in KGW is, on contrast, especially good for $^1D_2$ (table 1), which means that the mixing is small.

Figure 4 shows that $^1D_2$ multiplet consists of bands for which even at 7 K a certain structure can be observed. This suggests some distortions in the rare earth neighbourhood. Benefiting from the fact that the SOM model uses the crystallographic positions of the GdO_8 coordination polyhedra in the estimation of cfps, an attempt of evaluating a possible distortion that while affected $^1D_2$ keeps quite sharp the ^3F_J multiplets was performed. For this, a systematic shift between −10% and 10% with respect to the previously determined [11] positions of all oxygens, O1, O2 and O3, involved in the first coordination sphere of Gd^{3+}, was considered. Figure 10 presents the comparison of the evolution of $^1D_2$ and $^3F_3$ calculated energy level positions versus the displacements of O1, O2 and O3 ions.

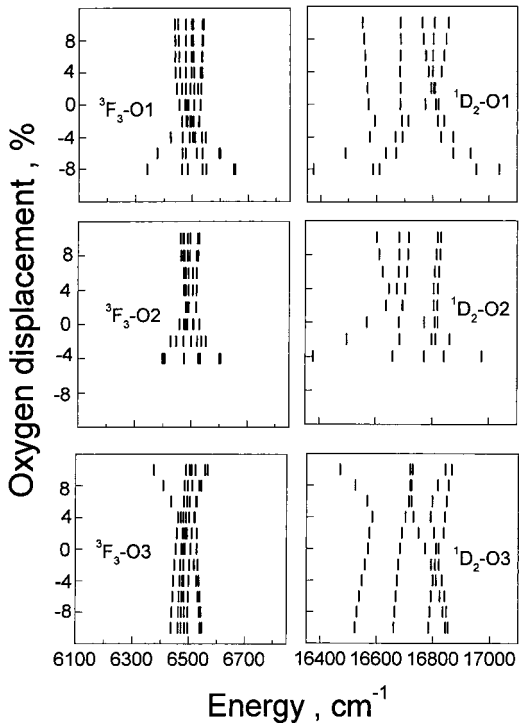

Figure 10. Evolution of the $^3F_3$ and $^1D_2$ energy levels calculated using the SOM model with respect to the displacement of O1, O2 and O3 oxygen ($\rho = 5\%$). For O1 and O2 some of them have not been represented because interatomic distances involved are not realistic.

These calculations indicate that the magnitudes of the energy shifts for the $^1D_2$ levels agree with the structure observed within the bandwidth in figure 7, the position of these levels being in any case much more sensitive to a considered oxygen displacement than that for the ^3F_J multiplets, but, while it is clear that distortion in the environment of Pr in the matrix may qualitatively explain differences in bandwidths between $^1D_2$ and ^3F_J multiplets, only a few considerations can be made at this stage in order to distinguish which RE–O bond has the largest influence. In any case, since displacements of O1 and O2 have effect over only one kind of interatomic distance, in each case, the change of these distances will influence *all* multiplets, although more important for $^1D_2$. In contrast, O3 is involved in two different RE–O bondings. The combination of crystal field effects arising from a supposed displacement, not necessarily important, of O3 introduces a minimum shift in the positions of ^3F_J levels, while those of $^1D_2$ change more significantly, explaining therefore the larger broadening of the $^1D_2$ bandwidth in comparison of those observed for ^3F_J multiplets.

5.3. Judd–Ofelt calculations

The Judd–Ofelt (JO) theory allows us to describe the 300 K optical absorption cross sections of lanthanides. The experimental oscillator strengths, f_{exp}, are calculated as

$$f_{exp} = \frac{2mc}{\alpha_f h N \bar{\lambda}^2} \Gamma_{JJ'} \tag{4}$$

where m is the electron mass, c the vacuum speed of the light, α_f the fine-structure constant, h the Planck constant, $\bar{\lambda}$ is the average wavelength of the $J \rightarrow J'$ transition and $\Gamma_{JJ'} = \int \alpha(\lambda) \partial\lambda$

Table 3. Room temperature integrated absorption cross sections $\int \alpha \partial\lambda$ divided by the dopant concentration, N, and average wavelength multiplet position, $\bar{\lambda}$.

$^{2S+1}L_J$	$N^{-1}\Gamma_{JJ'} \times 10^{28}$(300 K) ($cm^{+3}$) λ (300 K) (nm)		
	$\parallel g$	$\parallel m$	$\parallel p$
$^3H_6 + {}^3F_2$	1896	6778	4402
	2001	1993.2	1983.5
$^3F_3 + {}^3F_4$	1972	2761	2590
	1541.5	1550	1588
$^1D_2$	96	173	162
	596.6	596.6	598.3
$^3P_0$	0	137	0
		490.3	
$^3P_1 + {}^1I_6$	197	305	453
	479.8	479.5	480.3
$^3P_2$	270	475	444
	450.5	451.7	452.4

the integrated absorption. The room temperature $N^{-1}\Gamma_{JJ'}$ experimental values are summarized in table 3.

The standard JO theory yields the theoretical oscillator strength of ED transitions, $f_{ED,th}$ according to the expression

$$f_{ED,th} = \chi \left[\frac{8\pi^2 mc}{h}\right] \frac{1}{3\bar{\lambda}(2J+1)} S_{JJ'} \tag{5}$$

where $\chi = (n^2+2)^2/9n$ (n stands for the refractive index) and the line strengths are $S_{JJ'} = \sum_{k=2,4,6} \Omega_k |\langle \| U^\lambda \| \rangle|^2$. Ω_k are the adjustable JO parameters and the reduced matrix elements corresponding to the $J \rightarrow J'$ transition of Pr^{3+}, $\langle \| U^\lambda \| \rangle$, have been tabulated previously [16].

The application of the standard JO theory to Pr^{3+} often yields a large discrepancy between the experimental and theoretical oscillator strengths for the $^3H_4 \rightarrow {}^3P_2$ transition. The reason for this is the breaking of some of the assumptions of the JO theory, for instance the barycentre energy gap between the $4f^2$ and $4f^15d^1$ configurations is much smaller than in other lanthanide ions. Often the $^3H_4 \rightarrow {}^3P_2$ transition is ignored and the JO treatment is limited to transitions to multiplets with energy lower than $^3P_2$ [26]. In some cases modified JO theories [26, 27] are used to improve the agreement, the first introducing Ω_k parameters with k even and odd. The modified line strengths used in the last of these models are

$$S_{JJ'} = [1 + 2\alpha(E_J + E_{J'} - 2E(4f))] \sum_{k=2,4,6} \Omega_k |\langle \| U^\lambda \| \rangle|^2 \tag{6}$$

where $\alpha = 1/(2\Delta_{5d}) \approx 0.1 \times 10^{-4}$ cm. Δ_{5d} is the energy difference between the $4f^2$ and $4f^15d^1$ electron configurations of Pr^{3+}. E_J and $E_{J'}$ are the energies of the initial and final states respectively and $E(4f) \approx 9940\ cm^{-1}$ [27] is the mean energy of the 4f levels. We have considered the three methods to obtain the Ω_k set describing the Pr^{3+} spectroscopic properties in KGW.

The JO theory does not consider the crystal field of the lattice. Its application to anisotropic solids requires the average of the experimental optical properties. For this purpose we have treated separately the contributions of each polarization configuration and the $\Omega_k^{g,p,m}$ set has been calculated by minimizing the $\sum_{J'} (f_{exp} - f_{ED,th})^2$ differences. The $f_{ED,th}$ value

Table 4. Average JO parameters of Pr^{3+} in $KGd(WO_4)_2$ obtained for three models: (a) standard model without considering the oscillator strength of the $^3P_2$ multiplet; (b) standard model including the contribution of the $^3P_2$ multiplet; (c) using the modified line strengths given in equation (6), without considering the oscillator strength of the $^3P_2$ multiplet.

	(a)	(b)	(c)
$\bar{\Omega}_2 \times 10^{20}$ (cm^2)	12.0	11.8	19.50
$\bar{\Omega}_4 \times 10^{20}$ (cm^2)	8.15	8.06	7.31
$\bar{\Omega}_6 \times 10^{20}$ (cm^2)	2.64	3.00	4.86

corresponding to each JJ' multiplet has been calculated using the corresponding refractive indices, n_g, n_m and n_p of KGW at the corresponding $\bar{\lambda}$ of the multiplet [11]. An average $\bar{\Omega}_k = (\Omega_k^g + \Omega_k^m + \Omega_k^p)/3$ is used for further analyses of the photoluminescence. Table 4 shows a comparison of the $\bar{\Omega}_k$ values obtained.

The best agreement between our experimental and calculated oscillator strengths is achieved using the standard JO model without considering the contributing of the $^3P_2$ multiplet; however this leads only to minor changes in the Ω_k set in either of the cases of the standard JO model. On the other hand, the differences of the oscillator strengths calculated by the standard or modified models are not large when the $^3P_2$ contribution is included. It must be concluded that for KGW the three approaches yield similar radiative lifetimes.

5.4. De-excitation processes

The JO theory provides a method to evaluate the radiative properties of the rare earth ions by using the JO parameters. The radiative transition rates, $A_{JJ'}$, for the excited levels are expressed by

$$A_{JJ'} = \chi \left[\frac{32\pi^3 c\alpha_f}{3\bar{\lambda}^3} \right] \frac{n^2}{(2J+1)} S_{JJ'} \tag{7}$$

$S_{JJ'}$ being expressed according to the standard or modified model used.

Table 5 summarizes the radiative transitions rates calculated for the Pr^{3+} levels with energy equal to or lower than the $^3P_2$ multiplet using the standard line strengths. Table 5 also includes the luminescence branching ratio $\beta_{JJ'} = A_{JJ'} / \sum_{J'} A_{JJ'}$ and the radiative lifetimes $\tau_{rJ} = 1/\sum_{J'} A_{JJ'}$.

The radiative lifetimes of the $^3H_5$ multiplet calculated by the standard JO model without the $^3P_2$ contribution, $\tau = 59$ ms, is lower than that obtained using the modified model, $\tau = 62$ ms. With this exception, the radiative lifetimes obtained using the Ω_k set of the standard JO model are larger by a factor of 1–1.55 than those calculated in the modified one. The largest discrepancies between both models occur for the $^3P_2$ and $^1D_2$ multiplets. In these cases the values obtained are $\tau(^3P_2) = 66$ μs, $\tau(^1D_2) = 72.5$ μs and $\tau(^3P_2) = 45$ μs, $\tau(^1D_2) = 46.7$ μs for the standard and modified models respectively. This discrepancy could be expected from the lower agreement between the experimental and calculated oscillator strengths of these levels. The branching ratio of the $^1G_4 \rightarrow {}^3H_5$ (1.3 μm) emission is 0.48 and the expected radiative lifetime of the $^1G_4$ multiplet is similar to that found in other laser matrices [4]; therefore, there is a good perspective for light amplification in this channel.

The 15 K long lived experimental lifetime of the $^3P_0$ multiplet ($\tau = 65$ ns) is much shorter than the radiative lifetime calculated by the JO analysis ($\tau = 5.8$ μs). This result suggests that even at 15 K the decay of the $^3P_0$ level is strongly influenced by non-radiative processes. As the Pr–Pr distance at this concentration is large (≈4.3 nm), efficient energy transfer is not

Table 5. Radiative transition rates $A_{ED,JJ'}$, branching ratios, $\beta_{JJ'}$, and radiative lifetimes, τ_r, calculated with $\bar{\Omega}_2 = 12.0 \times 10^{-20}$ cm^2, $\bar{\Omega}_4 = 8.15 \times 10^{-20}$ cm^2, $\bar{\Omega}_6 = 2.64 \times 10^{-20}$ cm^2.

	$\bar{\lambda}$ (nm)	$A_{ED,JJ'}$ (s^{-1})	$\beta_{JJ'}$ (%)	τ_r (μs)
$^3P_2 \rightarrow {}^1I_6$	10 788	0	0	6.6
$^3P_1$	8306	9	0	
$^3P_0$	5531	15	0	
$^1D_2$	1840	112	0	
$^1G_4$	812	16 171	11	
$^3F_4$	660	31 605	21	
$^3F_3$	638	27 313	18	
$^3F_2$	586	18 036	12	
$^3H_6$	563	30 686	20	
$^3H_5$	508	19 101	12	
$^3H_4$	462	9158	6	
$^1I_6 \rightarrow {}^3P_1$	36 101	0	0	43.1
$^3P_0$	11 351	0	0	
$^1D_2$	2218	237	1	
$^1G_4$	878	12 282	53	
$^3F_4$	703	7595	33	
$^3F_3$	678	22	0	
$^3F_2$	620	246	1	
$^3H_6$	594	383	2	
$^3H_5$	534	48	0	
$^3H_4$	483	2377	10	
$^3P_1 \rightarrow {}^3P_0$	16 556	0	0	6.3
$^1D_2$	2363	131	0	
$^1G_4$	900	1362	1	
$^3F_4$	717	13 006	8	
$^3F_3$	691	53 278	33	
$^3F_2$	631	27 174	17	
$^3H_6$	604	3178	2	
$^3H_5$	542	35 169	22	
$^3H_4$	490	26 808	17	
$^3P_0 \rightarrow {}^1D_2$	2756	44	0	5.8
$^1G_4$	951	2417	1	
$^3F_4$	750	14 446	8	
$^3F_3$	721	0	0	
$^3F_2$	656	78 606	46	
$^3H_6$	627	4934	3	
$^3H_5$	560	0	0	
$^3H_4$	505	72 444	42	
$^1D_2 \rightarrow {}^1G_4$	1453	2014	15	72.5
$^3F_4$	1029	6807	49	
$^3F_3$	976	642	5	
$^3F_2$	860	1562	11	
$^3H_6$	811	1161	8	
$^3H_5$	703	62	1	
$^3H_4$	618	1554	11	
$^1G_4 \rightarrow {}^3F_4$	3532	36	4	971
$^3F_3$	2970	4	0	
$^3F_2$	2109	9	1	
$^3H_6$	1835	456	44	
$^3H_5$	1360	477	46	
$^3H_4$	1075	48	5	

Table 5. (Continued)

	$\bar{\lambda}$ (nm)	$A_{ED,JJ'}$ (s^{-1})	$\beta_{JJ'}$ (%)	τ_r (μs)
$^3F_4 \rightarrow {}^3F_3$	18 657	0	0	1292
$^3F_2$	5236	1	1	
$^3H_6$	3818	162	21	
$^3H_5$	2212	272	35	
$^3H_4$	1544	339	43	
$^3F_3 \rightarrow {}^3F_2$	7278	1	0	653
$^3H_6$	4801	34	2	
$^3H_5$	2509	538	35	
$^3H_4$	1684	958	63	
$^3F_2 \rightarrow {}^3H_6$	14 104	0	0	756
$^3H_5$	3830	83	6	
$^3H_4$	2190	1239	94	
$^3H_6 \rightarrow {}^3H_5$	5258	14	46	33 261
$^3H_4$	2593	16	54	
$^3H_5 \rightarrow {}^3H_4$	5115	17	100	59 289

expected. The relaxation to the $^1D_2$ low energy multiplet is the most likely mechanism for lifetime shortening.

The experimental $^1D_2$ lifetime at 15 K of the lowest Pr doped samples is $\approx$51 μs (see figure 9(b)): this value is slightly larger than the radiative lifetime calculated by the modified JO model; therefore, the standard JO model seems to give a more realistic approximation in our case. Using the radiative lifetime obtained in the standard JO model, we can calculate a low limit for the quantum efficiency of the $^1D_2$ emission at 10 K, $\eta = \tau_e/\tau_r = 0.56$.

The difference between radiative and experimental lifetimes is due to the presence of non-radiative processes, namely multiphonon emission and energy transfer, $\tau_{exp}^{-1} = \tau_r^{-1} + \tau_{ph}^{-1} + \tau_C^{-1}$, where τ_{ph}^{-1} is the multiphonon relaxation rate and τ_C^{-1} is the energy transfer rate. The temperature dependence of the multiphonon relaxation rate is given by [28]

$$\tau_{ph}^{-1}(T) = \tau_{ph}^{-1}(0)(1+n)^{ph} \tag{8}$$

where $n = [\exp(\bar{h}\omega/kT) - 1]^{-1}$, $\bar{h}\omega$ being the energy of the phonon emitted, often taken as the cutting frequency in the Raman or infrared spectra, k the Boltzmann constant and ph the number, not necessary an integer, of phonons required to maintain the energy conservation in a non-radiative transition between the levels separated by ΔE. The energy distance between the $^1D_2$ and the low-lying $^1G_4$ levels is $\Delta E = 6883\,\mathrm{cm}^{-1}$. Assuming that the phonon emitted is the largest one of the Raman spectrum of KGW, namely 901 cm^{-1}, the number of emitted phonons must be $ph = 7$ or 8. Figure 9(b) shows (continuous line) the fit obtained using equation (8) and assuming $ph = 8$. The multiphonon emission roughly describes the temperature dependence of the experimental lifetime although the experimental values are slightly shorter than those obtained in the fit. This difference may be due to the simultaneous emission of phonons with smaller energy.

The speeding up of the light intensity decays of the $^1D_2$ multiplet with Pr concentration (figure 9(a)) indicates the presence of energy transfer processes. The non-exponential character of the decays corresponding to high concentration can be described by the continuum model developed by Inokuti and Hirayama [29]. This model assumes energy transfer from an excited Pr^{3+} donor to the surrounding Pr^{3+} ions in the ground state continuously distributed. The light

Table 6. Average Pr–Pr distance, $\bar{r}$, for increasing Pr concentration, [Pr], and critical distance of the cross relaxation phenomena, R_C.

[Pr] nominal	$N \times 10^{-20}$ (cm^{-3})	$\bar{r}$ (nm)	R_C (nm)
0.1%	0.03	4.30	
1%	0.03	2.00	1.40
3%	0.9	1.38	1.41
5%	1.9	1.08	1.42

intensity decay follows the law

$$I(t) = I(0)\exp\left[\frac{-t}{\tau_0} - \Gamma\left(1-\frac{3}{s}\right)\frac{N}{c_0}\left(\frac{t}{\tau_0}\right)^{3/s}\right] \tag{9}$$

where $c_0 = 3/\Delta\pi R_C^3$ is a critical concentration related to the distance R_C at which the donor–trap energy transfer rate is equal to the spontaneous decay rate and $\Gamma(x)$ is the gamma function evaluated in x. $s = 6$, 8 or 10 corresponds to the transfer mechanism of electric dipole–dipole, dipole–quadrupole or quadrupole–quadrupole character respectively.

The character of the transfer mechanism can be deduced by plotting $\ln[I(t)/I(0)] + t/\tau_0$ versus $t^{3/s}$ and using the τ_0 value obtained for 0.1% Pr doped samples. The decays of 1–5% Pr doped samples fit linearly when $s = 6$. Therefore, an electric dipole–dipole transfer has taken place. Figure 9(a) shows the fit of the RT experimental decays of level $^1D_2$ using equation (9) with $s = 6$ and the corresponding praseodymium concentration. A very good fit is obtained for 1% and 3% Pr doped samples while the fit of the 5% Pr doped sample shows some deviation at the decay tail. This deviation is probably due to a minor contribution of electric dipole–quadrupole cross relaxation phenomena. The fits provide the critical distance, R_C, for each concentration. Table 6 summarizes the distances obtained. These critical distances can be compared with the average Pr–Pr distances $\bar{r} = (4\pi N/3)^{-1/3}$ for each sample. It is clear that the average Pr–Pr distance in the lowest doped samples is too large in comparison to the critical distance where the cross relaxation phenomena take place, namely $\approx$1.4 nm; therefore energy transfer does not occur and the decays can be expected to be single exponentials as indeed found. The average Pr–Pr distance decreases with increasing Pr concentration and it falls into the range where cross relaxation phenomena become activated, therefore the $^1D_2$ decays become non-exponential.

6. Conclusions

Oxygen displacements in the neighbourhood of Pr^{3+} induce centres with slightly different crystal fields which contribute to the spectroscopic properties of the average Pr^{3+} site in $KGd(WO_4)_2$ single crystals. 74 energy levels have been determined for this Pr^{3+} site and they have been successfully fitted with the cfp set of table 2. The standard Judd–Ofelt theory yields radiative lifetimes similar to those observed for the $^1D_2$ multiplet in the lowest concentration samples studied, [Pr]= 0.03×10^{20} cm^{-3}. For higher Pr concentrations the lifetime of this multiplet is shortened by electric dipole–dipole transfer between Pr donors and acceptors. Electrons excited to the $^3P_0$ multiplet are relaxed to the $^1D_2$ one even at low temperature.

Acknowledgments

This work is supported by CICyT under projects TIC96-1039 and MAT99-1077 and by MONOCROM SL (Spain). The authors acknowledge experimental help in lifetime

measurements at Universidad Autónoma de Madrid (C-IV). PP thanks the Betancourt Peronnet foundation for support.

References

[1] Kaminskii A A, Ueda K, Eichler H E, Findeisen J, Bagayev S N, Kuznetsov F A, Pavlyuk A A, Boulon G and Bougeois F 1998 *Japan. J. Appl. Phys.* **37** L293
[2] Chen Y, Major L and Kushawaha V 1996 *Appl. Opt.* **35** 3203
[3] Kaminskii A A, Li L, Butashin A V, Mironov V S, Pavyuk A A, Bagayev S N and Ueda K 1997 *Japan. J. Appl. Phys.* **36** L107
[4] Simons D R, Faber A J and de Waal H 1995 *Opt. Lett.* **20** 468
[5] Kuleshov N V, Shinkevich A S, Shcherbitsky V G, Mikhailov V P, Danger T, Sandrock T and Huber G 1996 *Opt. Mater.* **5** 111
[6] Mironov V S and Li L E 1998 *J. Alloys Compounds* **279** 83
[7] Wybourne B G 1965 *Spectroscopic Properties of Rare Earths* (New York: Wiley–Interscience)
[8] Hüfner S 1978 *Optical Spectra of Transparent Rare Earth Compounds* (New York: Academic)
[9] Judd B R 1962 *Phys. Rev.* **127** 750
[10] Ofelt G S 1962 *J. Chem. Phys.* **37** 511
[11] Pujol M C, Rico M, Zaldo C, Solé R, Nikolov V, Solans X, Aguiló M and Díaz F 1999 *Appl. Phys.* B **68** 187
[12] Solé R, Nikolov V, Ruiz X, Gavaldà Jna, Solans X, Aguiló M and Díaz F 1996 *J. Cryst. Growth* **169** 600
[13] Pujol M C, Solé R, Nikolov V, Gavaldá Jna, Massons J, Zaldo C, Aguiló M and Díaz F 1999 *J. Mater. Res.* **14** 3739
[14] Kunz M, Kretschmann H, Assmuss W and Klingshirn C 1987 *J. Lumin.* **37** 123
[15] de Mello-Donegá C, Meijerink A and Blasse G 1995 *J. Phys. Chem. Solids* **56** 673
[16] Weber M J 1968 *J. Chem. Phys.* **48** 4774
[17] Aumüller G C, Kostler W, Grabmaier B C and Frey R 1994 *J. Phys. Chem. Solids* **55** 767
[18] Carnall W T, Goodman G L, Rajnak K and Rana R S 1989 *J. Chem. Phys.* **90** 3443
[19] Görller-Walrand C and Binnemans K 1996 Rationalization of crystal-field parametrization *Handbook on the Physics and Chemistry of Rare Earths* vol 23, ed K A Gschneidner Jr and L Eyring (Amsterdam: North-Holland) p 121
[20] Garcia D and Faucher M 1995 Crystal field in non-metallic (rare earth) compounds *Handbook on the Physics and Chemistry of Rare Earths* vol 21, ed K A Gschneidner Jr and L Eyring (Amsterdam: North-Holland) p 263 (and references therein)
[21] Malta O L, Ribeiro S J L, Faucher M and Porcher P 1991 *J. Phys. Chem. Solids* **52** 587
[22] Porcher P 1989 Fortran routines REEL and IMAGE for simulation of d^N and f^N configurations involving real and complex crystal-field parameters, unpublished
[23] Görller-Walrand C and Binnemans K 1998 Spectral intensities of f–f transitions *Handbook on the Physics and Chemistry of Rare Earths* vol 25, ed K A Schneidner Jr and L Eyring (Amsterdam: Elsevier) pp 101–264
[24] Chang N C, Gruber J B, Leavitt R P and Morrison C A 1982 *J. Chem. Phys.* **76** 3877
[25] Garcia D and Faucher M 1989 *J. Chem. Phys.* **90** 5280
[26] Goldner P and Auzel F 1996 *J. Appl. Phys.* **89** 7972
[27] Kornienko A A, Kaminskii A A and Dunina E B 1990 *Phys. Status Solidi* b **157** 267
[28] Riseberg L A and Moss H W 1968 *Phys. Rev.* **174** 429
[29] Inokuti M and Hirayama F 1965 *J. Chem. Phys.* **43** 1978